Journal of Alloys and Compounds 509 (2011) 10222–10229

Contents lists available at SciVerse ScienceDirect

Journal of Alloys and Compounds

journal homepage: www.elsevier.com/locate/jallcom

Short-to-medium range order of Al–Mg metallic glasses studied by molecular dynamics simulations

C.C. Wang, C.H. Wong*

School of Mechanical & Aerospace Engineering, Nanyang Technological University, 50 Nanyang Avenue 639798, Singapore

ARTICLE INFO

Article history:
Received 20 June 2011
Received in revised form 20 August 2011
Accepted 22 August 2011
Available online 26 August 2011

Keywords:
Molecular dynamics (MD)
Metallic glasses
Atomic structure
Short range order
Medium range order

ABSTRACT

Molecular dynamics simulations of Al–Mg metallic glasses with a wide composition range have been conducted. We made use of a variety of analytical methods to study their amorphous structure. Pair distribution functions were constructed to determine the interatomic distances, and we found good agreement with reported simulation and experimental results. Coordination number analyses revealed that Mg atoms are more likely to serve as neighbour atoms in Al-centred icosahedral clusters in the middle concentration range or to form larger polyhedra at the Al-rich end. The presence of the 155-type pairs demonstrated that icosahedral ordering is predominant in the Al–Mg alloy. Results of Voronoi tessellation showed that Al-centred icosahedra are abundant in most compositions of the Al–Mg alloy and will lead to the formation of short-range order. The icosahedral clusters are highly shared with one another forming the medium-range order and there are less than 3% isolated icosahedra in most of the compositions of the Al–Mg alloy. Finally, the sharing schemes of icosahedra are represented by the splitting of the second peak of each pair distribution function.

1. Introduction

The atomic structures of metallic glasses (MGs) have received great attention in the past decade, due to its importance in understanding the glass-forming mechanism. Among the many MGs reported in the last few years, both Al-based and Mg-based MGs are the most common and they have been widely researched experimentally and theoretically [1–14] due to their lightweight and excellent mechanical properties [7,15,16]. One such Al-based MG is the Al–RE (rare element) bulk metallic glass (BMG) [17] of which numerous experimental studies have been performed on. Li et al. studied the reduced density functions from electron diffraction measurement of $Al_{89}La_6Ni_5$ MG [1]. They observed three different reduced density functions, with the first/second peaks respectively located at 2.76/3.32, 2.90/3.46 and 2.96/3.55 Å. The variations are due to the slight lengthening in the mean Al–Al, the larger lengthening of the Al–La first-neighbour contacts, and the shortening of the mean Al–Ni contact. Wei et al. successfully synthesized $Al_{75}Ni_{10}Ti_{10}Zr_5$ BMG by mechanical alloying and vacuum hot pressing with a high crystallization temperature of 790 K and a wide supercooled liquid region of 49 K [2]. The BMG exhibited high thermal stability and microhardness in the range of 790–850 HV. The deformation and fracture mechanisms of cold-rolled $Al_{87}Ni_7La_6$ were studied by Rizzi et al. [3]. They observed that the ribbons will break into fragments and form shear bands after a few rolling passes. Jiang and Atzmon examined the rate dependence of serrated flow in $Al_{86.8}Ni_{3.7}Y_{9.5}$ MG by nanoindentation [4]. The cold-rolled MG was found to form stable and time-dependent flow due to residual free volume trapped in the shear bands after its formation [4].

Several theoretical studies on Al-based MGs were also reported. Das et al. investigated the structure and structural relaxation of $Al_{80}Ni_{20}$ MG by molecular dynamics (MD) simulations [5]. Their $Al_{80}Ni_{20}$ model exhibited chemical short-range order (SRO), which is due to the preference of Ni atoms to have Al rather than Ni atoms as nearest neighbours. Wang et al. made use of ab initio MD simulation to investigate molten $Al_{60}Cu_{40}$ [6]. They found no one cluster-type predominates in the system, and that the most prevalent polyhedra found are distorted icosahedra.

Mg-based amorphous alloys have also been widely developed and analysed in experiments and computer simulations. The thermodynamics and kinetics of the $Mg_{65}Cu_{25}Y_{10}$ BMG were studied in the supercooled liquid state and at the glass transition [7]. It was found that the structure of this BMG is characterized by the temperature dependence of the viscosity, the relatively small specific heat capacity difference between liquid and crystal, and the pronounced heating rate dependence of the glass transition. Recently, Mg–Cu–Y–Ag BMGs were successfully generated by water cooled copper mould casting. When compared with $Mg_{65}Cu_{25}Y_{10}$ ternary system, these quaternary BMGs possessed improved mechanical

---

* Corresponding author. Tel.: +65 6790 5913.
E-mail address: chwong@ntu.edu.sg (C.H. Wong).

0925-8388/$ – see front matter
doi:10.1016/j.jallcom.2011.08.075

properties such as higher fracture stress at the expense of reduced thermal stability [8]. Another phase-separated $Mg_{60}Cu_{10}Ni_{16}Nd_{14}$ BMG with a diameter of over 3 mm was also developed. This sample possessed an enhanced compressive plastic strain about 2.5% due to phase-separated regions homogeneously distributed in the as-cast samples [9]. For theoretical calculations, Bailey et al. employed MD simulation methods to investigate the thermodynamics and structural properties of a wide composition range of Mg–Cu MGs [10]. It was found that the splitting of the second peak in the pair distribution function (PDF) is a natural consequence of narrowing and that the Mg–Cu MGs possessed fragile-liquid behaviour in supercooled regime. Gao et al. studied the structural evolution of $Mg_{65}Cu_{25}Y_{10}$ MG from 2000 K to 300 K by ab initio MD simulations and found distinct change in the structural characterization at around 750 K [11].

Additionally, theoretical investigations of Al–Mg binary MGs were also reported [12–14]. Liu et al. made use of MD simulations to study the formation properties of atomic clusters during rapid solidification processes for $Al_{50}Mg_{50}$ alloy [12]. They concluded that the Al–Mg amorphous structure is characterized with Al-centred icosahedral topological SRO during the rapid solidification processes. Hou et al. examined the short-to-medium range order of $Al_{50}Mg_{50}$ MG by adopting the MD method [13]. They found that the massive icosahedra in the $Al_{50}Mg_{50}$ supercooled liquid prevent it from crystallizing and play a critical role in the formation of MG. Wang and Liu studied the amorphous structure of $Al_{12}Mg_{17}$ alloy using MD simulations based on embedded-atom method (EAM) potentials derived by the force-matching approach [14]. The liquid structures were calculated and the structural factors were reported to be in good agreement with experimental data.

These theoretical studies, however, largely focused on a specific representative composition of the Al–Mg system. Furthermore, the analytical methods applied were primarily limited to PDFs, coordination numbers (CNs), and Honeycut–Andersen (H–A) indices [18,19]. In this paper, we made use of classical MD simulations and Voronoi tessellations [20], in addition to the above-mentioned structural characterization methods, to investigate the atomic structure of Al–Mg MGs. The results of this work will unravel the effect of alloying compositions on short-to-medium range order and the atomic structure of the Al–Mg MGs.

2. Computational model and analytical methods

In this work, we studied a wide composition range of Al–Mg amorphous alloys using classical MD simulations [21]. Each simulation model consisted of 2000 atoms and the many-body EAM potential [22,23] was adopted to describe the interatomic interactions in the simulation model. The EAM potential energy is computed as the sum of embedding energy functions and short-ranged pair-wise potential functions, and is given by [22]

$$E_{tot} = \sum_i F_i(\rho_i) + \frac{1}{2}\sum_i\sum_j \phi(r_{ij}), \tag{1}$$

where ϕ is the short-range pair, r_{ij} is the distance between atoms i and j, and ρ is the host density. In our simulations, the composition of Al atoms in the Al–Mg alloys varies from 50% to 95% in steps of 5%. Periodic boundary conditions were applied in the x-, y-, and z-directions of the simulation box and the system initial temperature was set at 1250 K. The system was then allowed to cool down rapidly from the equilibrated liquid state to 100 K at a cooling rate of 5×10^{11} K/s. In the simulations, the MD time step was set at 1 fs and Berendsen thermostat [24] was employed to regulate the initial temperature towards the desired temperature of 100 K. After each drop in the temperature, the system was then equilibrated under the isothermal isobaric (NPT) ensemble [25] with the external pressure set to 0. The configurations, atom coordinates, and the relevant properties were extracted at each equilibration stage for further investigations.

We adopted a range of analytical techniques to investigate the structure of a wide composition range of the amorphous Al–Mg alloy. Partial and total PDFs were employed to study the atomic arrangement. The partial PDF [26] is expressed as

$$g_{\alpha\beta}(r) = \frac{V}{N_\alpha N\beta}\left\langle \sum_{i}^{N}\sum_{j\neq i}^{N}\delta(r - r_{ij})\right\rangle, \tag{2}$$

where V is the volume of the system, and N_α and N_β are the number of atoms α and β, respectively. $\delta(r - r_{ij})$ is the Dirac delta function, and the angular brackets represent the time average. From the PDFs, we could determine the nearest neighbour shell and CNs. The H–A indices were then employed to identify and analyse the icosahedral ordering present in these systems. Three indices are used to describe different H–A pairs. The first index is 1 when two atoms are bonded to each other and is 2 if they are not. The second index is the number of nearest neighbours shared in common by the two atoms, and the third index is the number of bonds among the shared neighbour atoms. In general, a body-centred cubic structure is made up of 166-type and 144-type pairs, while face-centred cubic and hexagonal close packed structures consists of 142-type pairs [27]. In amorphous metals, however, a perfect icosahedron consists of 12 groups of 155-type pairs. If one of the pairs is broken, four of the 155-type pairs would transform into two 143-type pairs and two 154-type pairs, resulting in a distorted icosahedron [18,19,28].

We also made use of the Voronoi tessellation method to identify the number of i-edged ($i = 3, 4, 5, 6, \ldots$) faces n_i in a Voronoi cell by the Voronoi index $\langle n_3, n_4, n_5, n_6, \ldots\rangle$. An i-edged face reflects the local symmetry of the solute atom with some nearest-neighbour atoms in a certain direction. For instance, a perfect icosahedron is represented as $\langle 0, 0, 12, 0\rangle$ and if one 155-type pair is broken, it will result in a distorted icosahedron with a Voronoi index of $\langle 0, 2, 8, 2\rangle$.

3. Results and discussion

3.1. Pair distribution functions

Fig. 1 shows the PDFs for Al–Mg MGs with 10 different compositions, of which (a) shows the total PDFs, (b), (c) and (d) illustrate the partial PDFs for the Al–Al, Al–Mg, and Mg–Mg pairs, respectively. All the total and partial PDFs exhibit sharp and prominent first peaks with the exception of $Al_{90}Mg_{10}$ and $Al_{95}Mg_5$ alloys in which their first peaks in the Mg–Mg partial PDFs are significantly less distinct due to the low concentration of Mg element.

The PDFs can also be used to obtain the interatomic distance, which is defined as the radial distance corresponding to the first peak. According to Fig. 1, the interatomic distances of the Al–Al bond (2.8 Å), Al–Mg bond (3.05 Å) and Mg–Mg bond (3.2 Å) do not change significantly with different compositions of the systems. The interatomic distances of all the partial pairs show good agreement with both simulation and experimental results [5,12,14,29,30]. However, the first peak of the total PDF decreases from 3.05 Å to 2.95 Å as the concentration of Al increases from 50% to 95% (see Fig. 1(a)). This is due to the smaller radius of Al atom compared to that of a Mg atom ($R_{Al} = 1.43$ Å, $R_{Mg} = 1.6$ Å). As the concentration of Al increases, there will be a greater number of Al atoms in the system. As a result, the average interatomic distance for the whole system therefore decreases.

From Fig. 1, we also observe a prominent split in the second peak of each system. This signifies the presence of medium-range order (MRO), which will be discussed in further detail in Section 3.6.

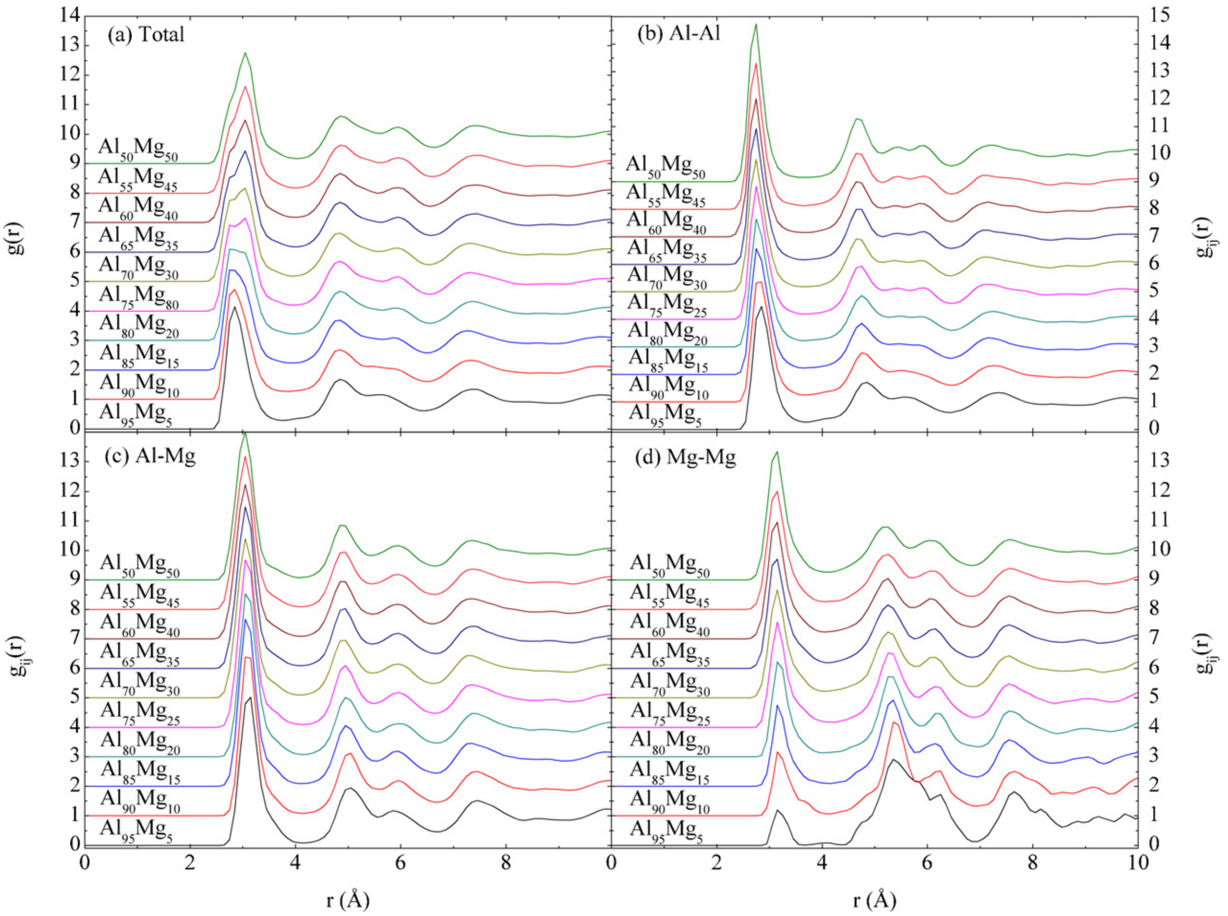

Fig. 1. PDFs for $Al_xMg_{(100-x)}$ MGs. (a) is the total PDFs of the whole system. (b), (c), and (d) are the partial PDFs of Al–Al, Al–Mg, and Mg–Mg pairs. Individual curves for different compositions are displaced vertically for clarity.

From the PDFs, we have also computed the cutoff value of the first shell, which is set as the minimum after the first peak (cutoffs of the Al–Al pair, Al–Mg pair, and Mg–Mg pair are 3.8 Å, 4.1 Å, and 4.1 Å, respectively). These values were used for computing the CNs and H–A indices.

3.2. Coordination number

Coordination number (CN) is the number of atoms that are in the nearest-neighbour shell of a given solute atom. Table 1 shows the partial and total CNs for different compositions of the Al–Mg alloy. According to the table, as the concentration of Al atoms increases, CN_{Al} and CN_{Mg} exhibit an increasing trend, while CN_{all} decreases slightly. The partial CNs, such as CN_{Al-Al} and CN_{Mg-Al}, increase with growing concentration of Al atoms, while CN_{Mg-Mg} and CN_{Al-Mg} drop. We also deduce that systems with approximately equal concentrations of Al and Mg favour unlike bonds due to strong chemical SRO as evidenced by the high CN_{Al-Mg} value.

Table 1
Coordination numbers in Al–Mg MGs.

Alloys	CN_{Al-Al}	CN_{Al-Mg}	CN_{Mg-Mg}	CN_{Mg-Al}	CN_{Al}	CN_{Mg}	CN_{all}
$Al_{50}Mg_{50}$	5.39	6.97	7.10	6.97	12.36	14.07	13.22
$Al_{55}Mg_{45}$	5.53	6.77	6.16	8.27	12.30	14.43	13.26
$Al_{60}Mg_{40}$	6.14	6.21	5.30	9.31	12.34	14.60	13.25
$Al_{65}Mg_{35}$	6.88	5.57	4.54	10.33	12.45	14.87	13.30
$Al_{70}Mg_{30}$	7.64	4.87	3.76	11.36	12.51	15.12	13.29
$Al_{75}Mg_{25}$	8.41	4.17	2.90	12.51	12.58	15.41	13.29
$Al_{80}Mg_{20}$	9.29	3.40	2.02	13.61	12.70	15.63	13.28
$Al_{85}Mg_{15}$	10.24	2.58	1.23	14.60	12.82	15.83	13.27
$Al_{90}Mg_{10}$	11.16	1.70	0.74	15.28	12.86	16.02	13.18
$Al_{95}Mg_5$	12.07	0.84	0.16	16.02	12.92	16.18	13.08

The distributions of Al-centred and Mg-centred coordination clusters were also analysed and shown in Fig. 2. According to Fig. 2(a), the Al-centred clusters are dominated by CN = 12 and 13 clusters. The abundance of CN = 12 clusters provides a good foundation for icosahedral ordering. However, with increasing Al concentration, the amount of CN = 12 clusters reduces while that of CN = 13 clusters increases. This is because, as the concentration of Al increases, some neighbour spaces of Al solute atom originally occupied by Mg solvent atoms are replaced with Al solvent atoms. Since Al atom has a smaller radius than an Mg atom, more Al solvent atoms are therefore needed to fill in the space and subsequently clusters with CN = 13 and greater are formed. Referring to Fig. 2(b), the distribution of Mg-centred coordination clusters is significantly different from those of Al-centred coordination clusters. In Mg-centred clusters, there is less than 10% of CN = 12 clusters. This low number of CN = 12 clusters prevents the Mg atoms from forming an abundance of icosahedra. This suggests that Mg atoms are more likely to function as neighbour atoms in Al-centred icosahedral clusters at around 55% Al concentration or to form larger polyhedra at the Al-rich end.

3.3. Common neighbour analysis

Fig. 3 shows the distribution of H–A indices for different concentrations of Al–Mg binary alloys. Although 155-type pairs are dominant in all compositions of Al–Mg binary alloys, they are sensitive to minor variations in the concentration. As the composition

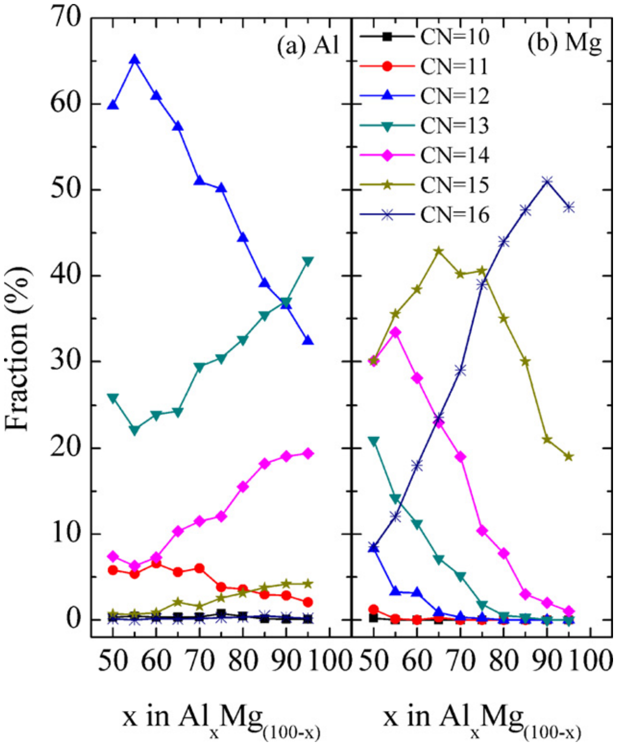

Fig. 2. Distribution of (a) Al-centred and (b) Mg-centred coordination clusters.

changes from $Al_{50}Mg_{50}$ to $Al_{65}Mg_{35}$, the fraction of 155-type pairs increases, peaking at around 57% in the $Al_{65}Mg_{35}$ system. As Al concentration continues to increase, the fraction of 155-type pairs begins to decrease, with the most significant drop occurring when the composition changes from $Al_{85}Mg_{15}$ to $Al_{95}Mg_5$. Despite the sensitivity to changes in the composition, the strong presence of 155-type pairs shows that icosahedral ordering is predominantly present in this wide composition range of Al–Mg alloys. Additionally, unlike the 155-type pairs, 154- and 143-type pairs increase as the Al concentration increases. This further suggests that broken 155-type pairs, which lead to a decline in the number of 155-type pairs, will be transformed into 154- or 143-type pairs.

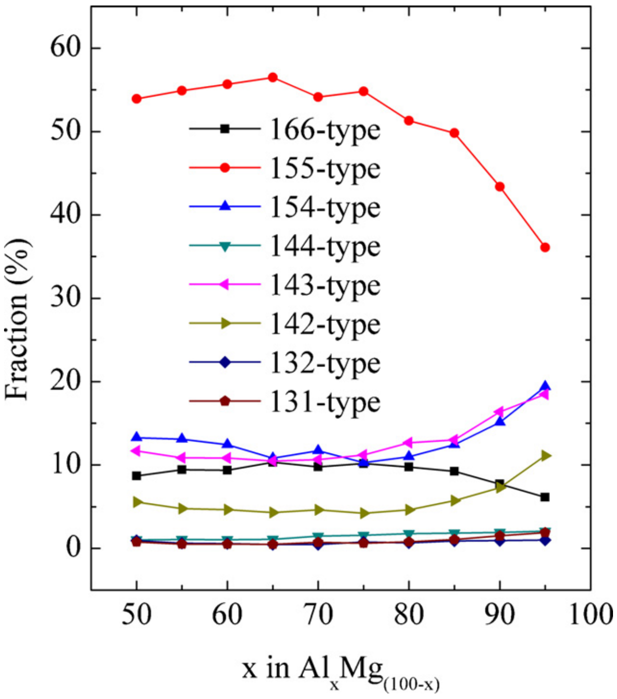

Fig. 3. H–A indices distribution for $Al_xMg_{(100-x)}$ MGs.

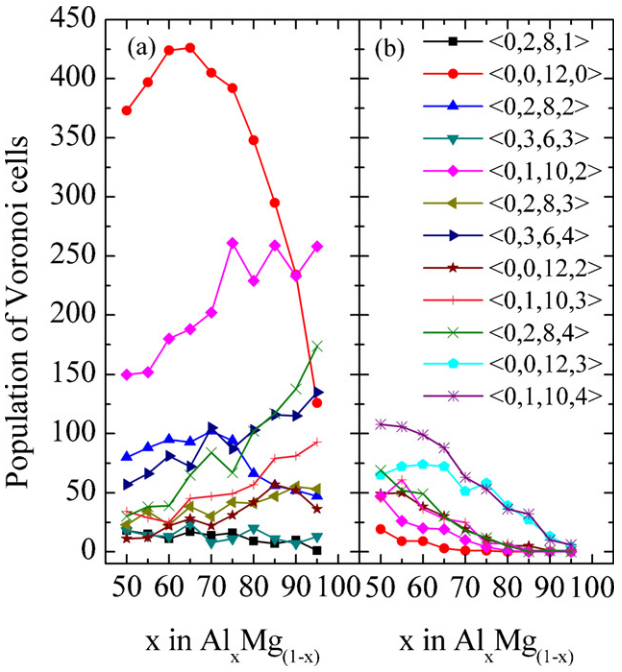

Fig. 4. Distribution of Voronoi indices in (a) Al-centred and (b) Mg-centred polyhedra.

3.4. Short-range order

The Voronoi tessellation method was used to verify important results obtained above and introduce some new phenomena. Fig. 4(a) and (b) shows the distribution of 12 most common types of Voronoi indices found in Al-centred and Mg-centred polyhedra. Among the various polyhedra around Al, the Al-centred full icosahedra with Voronoi index ⟨0, 0, 12, 0⟩ constitute the most populous structural unit. For example, there are more than 350 full icosahedra when the Al concentration is 80% or lower. Also, we see that the number of Z11 Kasper polyhedra [31] (only ⟨0, 2, 8, 1⟩) and Z10 (not shown in the figure), which are made up of fragments of incomplete, irregular or distorted icosahedra, is quite small. This is significantly different from the published results [6,32,33], which reported an abundance of Z10 and Z11 Kasper polyhedra in different systems. The low number of Z10 and Z11 Kasper polyhedra in our simulations is due to the presence of a large number of icosahedra, which are more structurally favourable. Although Al-centred icosahedra form in large numbers to dominate the Al–Mg structure, only a very small number of Mg-centred icosahedra are found (see Fig. 4(b)). Specifically, when the concentration of Al is more than 70%, no Mg-centred icosahedron is present in the system. Furthermore, all Voronoi cells in which the corresponding CNs are less than 15, decrease with decreasing Mg concentration. As a result, some large clusters with CNs of more than 16 are formed.

We also investigated the neighbour compositions of Al-centred full icosahedra since they are populous in the Al–Mg binary alloys. As illustrated in Fig. 5, there is a good mixture of Al and Mg atoms in the neighbour space of an Al-centred icosahedron for all Al concentrations except for concentrations of 85%, 90% and 95%. In these three systems, some icosahedra are made up of entirely 12 Al neighbour atoms, which is represented by the ‘12–0’ bar in Fig. 5, while other icosahedra are made up of more Al atoms than Mg atoms

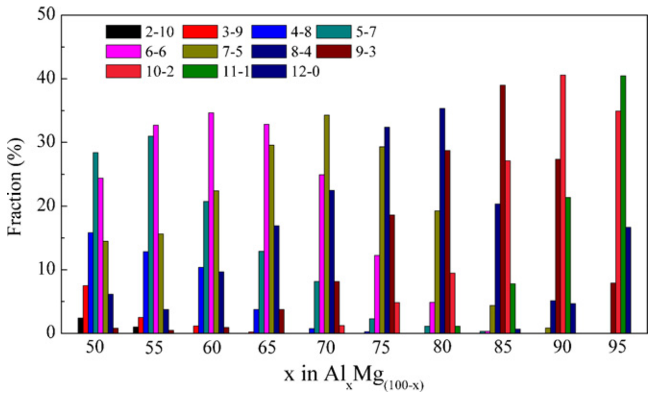

Fig. 5. Number of Al and Mg atoms in the neighbour space of Al-centred icosahedra in Al$_x$Mg$_{(100-x)}$ MGs.

(such as ‘8–4’, ‘9–3’, ‘10–2’, and ‘11–1’). However, the neighbour spaces in the other seven systems, i.e., Al concentrations ranging from 50% to 80%, consist of a larger number of Mg atoms (such as ‘5–7’, ‘6–6’, and ‘7–5’) compared to the three systems. Referring to Fig. 4(a) again, one can see that Al-centred icosahedra are more dominant in Al concentrations between 50% and 80%. Therefore, this implies that more Mg atoms located at the nearest neighbour shell will help facilitate the formation of icosahedra. In other words, icosahedra will not be formed easily if there are an insufficient number of Mg atoms in the neighbour space, such as those of Al–Mg systems with Al concentrations between 85% and 95%.

We also analysed the number of atoms that are part of the full icosahedra and presented the results in Table 2 (also see Fig. 6(e) for Al$_{55}$Mg$_{45}$). From the table, it shows that more than 80% of the atoms are part of any icosahedron when Al concentrations are below 85%. Therefore, it can be concluded that icosahedra are the primary SRO in these MGs. Icosahedra are distinctly present in these systems mainly because of two reasons. Firstly, the effective atomic size ratio between the solute atoms R_{Al} and solvent atoms R_{Mg} is 0.894, which is close to the ideal effective atomic size ratio of 0.902 for icosahedral packing [34]. Secondly, from the energetic point of view, it has been reported that icosahedral clusters have the least formation energy when compared with other icosahedral-like clusters [35]. Therefore, they are much easier to form and their structures are more stable than other clusters in amorphous alloys. Nevertheless, it is impossible for all atoms to be part of any icosahedral cluster since some glue atoms are needed to connect the clusters [36].

3.5. *Medium-range order*

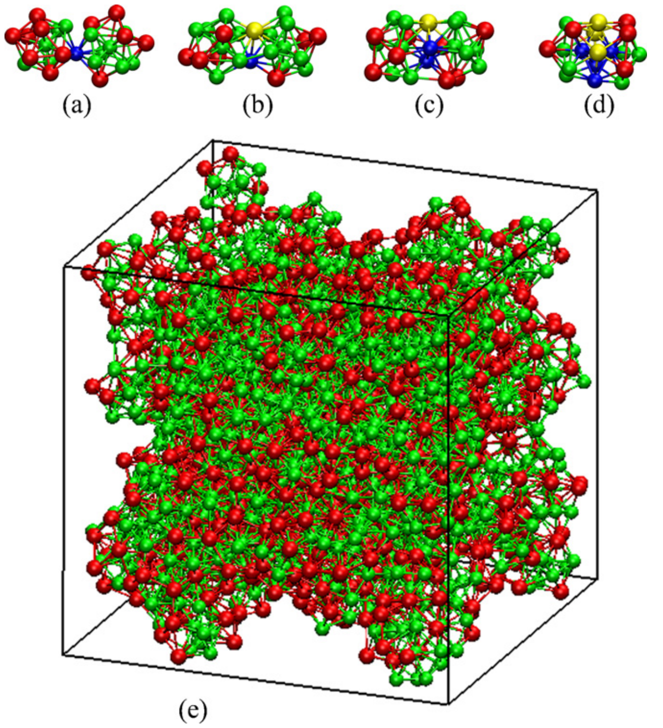

Fig. 6. Illustrations of (a) vertex, (b) edge, (c) face, (d) interpenetrating sharing modes in Al–Mg alloy, and (e) full icosahedra in Al$_{55}$Mg$_{45}$ system made up of 1743 atoms. Blue and yellow balls represent Al and Mg atoms respectively in (a)–(d). Green and red balls represent Al and Mg atoms, respectively in (e). (For interpretation of the references to color in the figure caption, the reader is referred to the web version of the article.)

Conventionally, the structural features beyond the first peak in the PDF to a distance up to 1–2 nm are called the MRO. Most icosahedra are connected or overlapped with other clusters by sharing solvent atoms, and this constitutes to MRO in these systems. If two full icosahedra are connected by sharing only one neighbour atom, it is defined as vertex sharing (VS, see Fig. 6(a)). If they share two connected atoms, it forms edge sharing (ES, see Fig. 6(b)). If three atoms forming a triangle are shared by two full icosahedra, it is defined as face sharing (FS, see Fig. 6(c)). If two full icosahedra share 5 common neighbour atoms and the two centre atoms are also neighbour of each other, it is known as interpenetrating icosahedra or tetrahedral bipyramid sharing (TS, see Fig. 6(d)). If a full icosahedron does not share any atom with others, it is known as an isolated full icosahedron.

Table 3 lists the sharing frequencies between two icosahedra. According to the table, VS occurs most frequently, while ES is the least. Also, systems possessing good icosahedral-forming ability exhibit higher sharing frequencies between the clusters. If icosahedra are the predominant structure in a system, they will be able to interact and connect with other clusters easily. On the contrary,

Table 2
Number of atoms in icosahedra of Al–Mg MGs. N_{all}, N_{Al} and N_{Mg} represent the number of all atoms, Al atoms, and Mg atoms respectively that are part of icosahedral clusters. F_{Al} and F_{Mg} are the at.% of Al and Mg atoms, respectively. Values in parentheses are for isolated icosahedral clusters where there is no sharing.

Alloys	N_{all}	N_{Al}	N_{Mg}	F_{Al}	F_{Mg}
Al$_{50}$Mg$_{50}$	1717 (5096)	862 (2467)	855 (2629)	50.20% (48.41%)	49.80% (51.59%)
Al$_{55}$Mg$_{45}$	1743 (5278)	928 (2644)	815 (2634)	53.24% (50.09%)	46.76% (49.91%)
Al$_{60}$Mg$_{40}$	1747 (5629)	1021 (3016)	726 (2613)	58.44% (53.58%)	41.56% (46.42%)
Al$_{65}$Mg$_{35}$	1769 (5577)	1114 (3230)	655 (2347)	62.97% (57.92%)	37.03% (42.08%)
Al$_{70}$Mg$_{30}$	1741 (5278)	1176 (3244)	565 (2034)	67.55% (61.46%)	32.45% (38.54%)
Al$_{75}$Mg$_{25}$	1749 (5109)	1277 (3405)	472 (1704)	73.01% (66.65%)	26.99% (33.35%)
Al$_{80}$Mg$_{20}$	1640 (4524)	1263 (3197)	377 (1327)	77.01% (70.67%)	22.99% (29.33%)
Al$_{85}$Mg$_{15}$	1607 (3835)	1332 (2989)	275 (846)	82.89% (77.94%)	17.11% (22.06%)
Al$_{90}$Mg$_{10}$	1467 (3042)	1289 (2552)	178 (490)	87.87% (77.94%)	12.13% (22.06%)
Al$_{95}$Mg$_5$	1005 (1638)	929 (1469)	76 (169)	92.44% (89.68%)	7.56% (10.32%)

Table 3
Sharing frequencies between two icosahedra in Al–Mg MGs. N_{VS}, N_{ES}, N_{FS}, N_{TS} are sharing frequencies of vertex, edge, face, and interpenetrating icosahedra, respectively.

Alloys	N_{VS}	N_{ES}	N_{FS}	N_{TS}
$Al_{50}Mg_{50}$	869	240	742	585
$Al_{55}Mg_{45}$	853	234	786	597
$Al_{60}Mg_{40}$	1054	319	949	683
$Al_{65}Mg_{35}$	1023	318	890	628
$Al_{70}Mg_{30}$	961	289	831	580
$Al_{75}Mg_{25}$	865	253	735	550
$Al_{80}Mg_{20}$	723	218	650	462
$Al_{85}Mg_{15}$	458	126	389	323
$Al_{90}Mg_{10}$	312	99	239	202
$Al_{95}Mg_{5}$	108	26	85	65

if there are only a few icosahedra in the system, they are likely to be separated by other form of clusters.

We studied the various sharing modes in greater details to understand and gain insight knowledge of the relationship between icosahedral-forming ability and the sharing modes. Fig. 7 shows the frequencies of VS, ES, FS and TS that occur in different compositions of the Al–Mg binary alloys. We observe from the figure that systems with Al concentration between 50% and 80% tend to possess very similar trends, while the plots of $Al_{85}Mg_{15}$, $Al_{90}Mg_{10}$, and $Al_{95}Mg_{5}$ systems deviate substantially away from the other systems. In these three particular systems, there exists a high fraction of isolated full icosahedra. For instance, more than half of the full icosahedra in $Al_{95}Mg_{5}$ neither exhibit VS, ES, FS nor TS with other clusters. And this translates to a total of about 20% isolated full icosahedra in the $Al_{95}Mg_{5}$ system as shown in Fig. 8(a), which illustrates the total cluster-sharing frequencies.

We also observe from Fig. 4 that these three particular systems possess weaker icosahedral-forming ability compared to other systems. Hence, instead of analysing the individual plot of each Al–Mg alloy that has good icosahedral-forming ability (i.e., Al concentration of 50–80%) in Fig. 7, we collated the data and illustrated their trends in Fig. 8(b). According to the figure, there is a high fraction of full icosahedra that do not exhibit ES with adjacent full icosahedra. Additionally, only 2.5% of the full icosahedra are isolated. These suggest that the presence of MRO is evident in these clusters, which is facilitated by sharing the shell atoms via the VS, ES, FS, and TS modes.

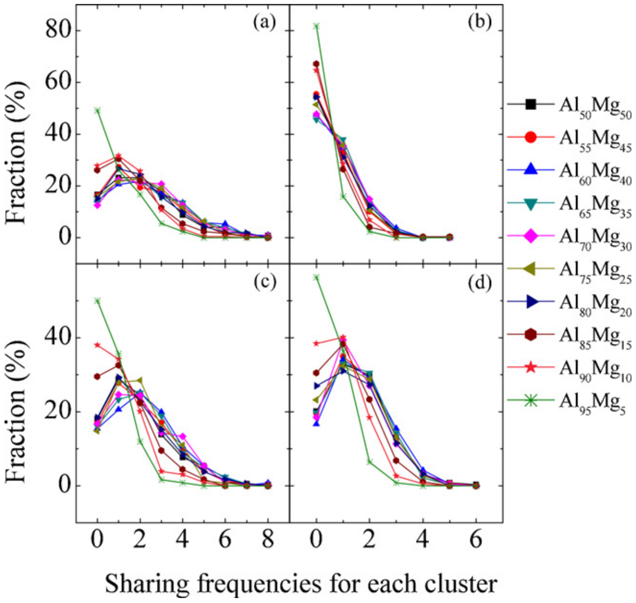

Fig. 7. Frequencies of (a) vertex, (b) edge, (c) face, and (d) tetrahedral bipyramid sharing of each icosahedron for various compositions of Al–Mg MGs.

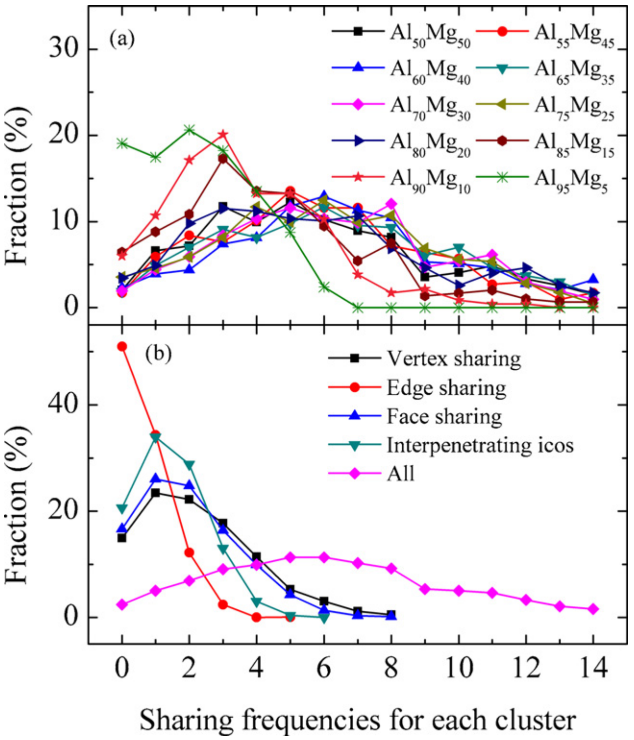

Fig. 8. Plots of (a) total sharing frequencies of each icosahedron for various compositions of Al–Mg MGs and (b) trend lines of sharing frequencies for different sharing modes.

However, why are there intensive sharings between these full icosahedra? Our results show that by sharing the shell atoms between the clusters, it allows the system to achieve atomic percentages of Al and Mg atoms in the icosahedral clusters closer to the composition of the system. This leads to improved stability of the system, which is highly desirable. For example, there are 406 icosahedra in $Al_{55}Mg_{45}$ (see Fig. 4). If all of these 406 icosahedra are isolated, then there will be a total of 5278 atoms forming the icosahedra. Out of these 5278 atoms, 2644 (F_{Al} = 50.09%) would be Al atoms and 2634 (49.91%) Mg atoms (see Table 2), which are significantly different from the expected 55% Al and 45% Mg in the system. This indicates that the system is unstable. However, our simulation results show that the icosahedra are made up of only 1743 atoms (928 Al atoms and 815 Mg atoms). This lower quantity is made possible by sharing the shell atoms between the full icosahedral clusters. Therefore, out of the 1743 atoms, 53.24% are Al atoms and 46.76% are Mg atoms. These percentages are closer to the composition of $Al_{55}Mg_{45}$ system providing better stability and there are only a small number of atoms that are not part of any icosahedral clusters.

Due to the reasons above, an icosahedral cluster in a MG, which possesses good icosahedral-forming ability, will consist of very few unique atoms that are not shared. Furthermore, these icosahedral clusters tend to be connected with one another in abundance. As a result, MRO will be formed and can exist either in rings by spherical-periodic order [37] or networks [32]. Additionally, the presence of the MRO enhances the static structure of the system.

Finally, the sharing modes of icosahedra could also be related to the origin of the polyamorphism [38] in the MGs. The polyamorphic phase transitions take place with the change in sharing intensity between icosahedral clusters in MGs. Additionally, there are less icosahedra in the temperature range above the liquidus temperature than in the glassy state. Although isolated icosahedra could

Table 4
Statistical distances between centre atoms of two icosahedra connected by vertex, edge and face sharing.

Alloys	R_{VS} (Å)	R_{ES} (Å)	R_{FS} (Å)
$Al_{50}Mg_{50}$	5.86	5.37	4.73
$Al_{55}Mg_{45}$	5.87	5.38	4.74
$Al_{60}Mg_{40}$	5.86	5.38	4.73
$Al_{65}Mg_{35}$	5.84	5.36	4.72
$Al_{70}Mg_{30}$	5.84	5.33	4.71
$Al_{75}Mg_{25}$	5.80	5.29	4.69
$Al_{80}Mg_{20}$	5.82	5.30	4.68
$Al_{85}Mg_{15}$	5.74	5.22	4.65
$Al_{90}Mg_{10}$	5.74	5.18	4.65
$Al_{95}Mg_{5}$	5.73	5.10	4.63
Average	5.81	5.29	4.69

be predominant in the temperature range above the liquidus temperature, the correlated icosahedra might be predominant in the supercooled liquid range around glass transition temperature T_g. Between the two regions there could be a structural transition that explains the thermodynamics [39] and causes the fragile-to-strong transition [40]. This is of considerable interest and remains to be systematically explored by MD simulations on the liquid structure.

3.6. Second peak splitting

MGs are formed from liquid with a rapid quenching rate. The obvious splitting of the second peak in the PDF, which cannot be seen in liquids, has been recognised as a typical indication of amorphous state [41]. This splitting has been regarded as the consequence of local ordering [42,43]. In this paper, we analyse the splitting of the second peak in the Al–Al PDFs through the sharing mechanisms between the full icosahedra, since Al-centred full icosahedra are highly prominent with the Mg atoms serving as neighbour atoms in most of the Al–Mg systems.

Table 4 lists the statistical distances between the centre atoms of two icosahedra connected by the VS, ES, and FS schemes of various compositions of the Al–Mg binary alloy. For interpenetrating icosahedra, the distance between two centre atoms is simply computed as the interatomic distance of the Al–Al bond. Therefore, it is not reflected in the second peak. Referring to Fig. 1(b), we observe three distinct sub-peaks in the second peak except for the $Al_{90}Mg_{10}$ and $Al_{95}Mg_5$ systems, in which icosahedral ordering is not predominant. Interestingly, the distance values corresponding to these three sub-peaks are 4.7 Å, 5.4 Å and 5.8 Å, which are close to the average statistical distances of 4.69 Å, 5.29 Å and 5.81 Å listed in Table 4. These sub-peaks are, therefore, due to the FS, ES and VS schemes. However, only two sub-peaks are observed in the $Al_{90}Mg_{10}$ and $Al_{95}Mg_5$ systems. This is probably due to the weak ES between the icosahedral clusters. As a result, the second sub-peak merges with the third sub-peak to form a single sub-peak. Therefore, only two obvious sub-peaks are seen in the PDFs of the $Al_{90}Mg_{10}$ and $Al_{95}Mg_5$ systems.

The results in this study are also consistent with the complex atomic configuration in MGs characterized by the combination of spherical-periodic order and local translational symmetry [43]. According to Ref. [43], the second peak is regarded as two sub-peaks. The ratio of the distance of the first sub-peak in the second peak to the first peak, R_{21}/R_1, is reported to be 1.73 Å, and the ratio of the distance of the second sub-peak in the second peak to the first peak, R_{22}/R_1, is reported to be 2.0 Å. Based on Fig. 1(b) and Table 4, we calculated $R_{FS}/R_1 = 1.68$ Å, $R_{ES}/R_1 = 1.89$ Å and $R_{VS}/R_1 = 2.07$ Å. The R_{FS}/R_1 value is in good agreement with the reported $R_{21}/R_1 = 1.73$ Å. By averaging the R_{ES}/R_1 and R_{VS}/R_1, we obtain the second sub-peak value over first peak (1.98 Å), which is close to the reported $R_{22}/R_1 = 2.0$ Å.

4. Conclusions

We have systematically studied a wide composition range of Al–Mg amorphous alloys by employing classical MD simulations with EAM many-body potential. PDFs have been constructed and verified with published literatures. According to the CN analyses, Mg atoms are likely to function as neighbour atoms in Al-centred icosahedral clusters or to form larger polyhedra at high Al concentrations. The common neighbour analyses show that 155-type pairs are dominant in all compositions of Al–Mg binary alloys, even though they are sensitive to any variations in the composition. Furthermore, the strong presence of 155-type pairs demonstrates that icosahedral ordering is dominant in all composition ranges of Al–Mg alloys. The Voronoi tessellation analysis shows that icosahedra are the primary means of SRO. It is also observed that polyhedra constructed by a larger number of Mg atoms in the neighbour space are easier to form full icosahedra. It has also been demonstrated that strong sharing mechanisms (VS, ES, FS, and TS) are present in the icosahedra to form MRO. The intensity of the MRO is sensitive to the number of icosahedra in the system. More icosahedra will result in stronger MRO. Finally, it has been proven that the splitting of second peak in the PDF is due to the sharing modes between the icosahedral clusters. Face sharing constitutes to the first sub-peak of the second peak in PDF, while ES and VS yield the second sub-peak.

References

[1] G.Q. Li, K.B. Borisenko, Y.X. Chen, D. Nguyen-Manh, E. Ma, D.J.H. Cockayne, Acta Mater. 57 (2009) 804–811.
[2] X. Wei, F.S. Han, X.F. Wang, X.F. Wang, C.E. Wen, J. Alloys Compd. 501 (2010) 164–167.
[3] P. Rizzi, A. Habib, A. Castellero, L. Battezzati, J. Alloys Compd. 509S (2011) S275–S278.
[4] W.H. Jiang, M. Atzmon, J. Alloys Compd. 509 (2011) 7395–7399.
[5] S.K. Das, J.H. Horbach, T. Voigtmann, Phys. Rev. B 78 (2008) 064208.
[6] S.Y. Wang, M.J. Kramer, M. Xu, S. Wu, S.G. Hao, D.J. Sordelet, K.M. Ho, C.Z. Wang, Phys. Rev. B 79 (2009) 144205.
[7] R. Busch, W. Liu, W.L. Johnson, J. Appl. Phys. 83 (1998) 4134–4141.
[8] X. Hui, G.Y. Sun, C.M. Zhang, S.N. Liu, E.R. Wang, M.L. Wang, G.L. Chen, J. Alloys Compd. 504S (2010) S6–S9.
[9] Y.L. Ren, R.L. Zhu, J. Sun, J.H. You, K.Q. Qiu, J. Alloys Compd. 493 (2010) L42–L46.
[10] N.P. Bailey, J. Schiotz, K.W. Jacobsen, Phys. Rev. B 69 (2004) 144205.
[11] R. Gao, X. Hui, H.Z. Fang, X.J. Liu, G.L. Chen, Z.K. Liu, Comput. Mater. Sci. 44 (2008) 802–806.
[12] F.X. Liu, R.S. Liu, Z.Y. Hou, H.R. Liu, Z.A. Tian, L.L. Zhou, Ann. Phys. 324 (2009) 332–342.
[13] Z.Y. Hou, L.X. Liu, R.S. Liu, Z.A. Tian, J.G. Wang, J. Non-Cryst. Solids 357 (2011) 1430–1436.
[14] L.H. Wang, H.Z. Liu, J. Non-Cryst. Solids 352 (2006) 2880–2884.
[15] A. Inoue, Prog. Mater. Sci. 43 (1998) 365–520.
[16] U. Wolff, N. Pryds, E. Johnson, J.A. Wert, Acta Mater. 52 (2004) 1989–1995.
[17] Y.Q. Cheng, E. Ma, Prog. Mater. Sci. 56 (2011) 379–473.
[18] H. Jónsson, H.C. Anderson, Phys. Rev. Lett. 60 (1988) 2295–2298.
[19] A.S. Clarke, H. Jónsson, Phys. Rev. E 47 (1993) 3975–3984.
[20] G.F. Voronoi, J.R. Angew, Mathematika 134 (1908) 198–287.
[21] S. Plimpton, J. Comp. Phys. 117 (1995) 1–19.
[22] M.S. Daw, M.I. Baskes, Phys. Rev. B 29 (1984) 6443–6453.
[23] M.I. Mendelev, M. Asta, M.J. Rahman, J.J. Hoyt, Phil. Mag. 89 (2009) 3269–3285.
[24] H.J.C. Berendsen, J.P.M. Postma, W.F. van Gunsteren, A. DiNola, J.R. Haak, J. Chem. Phys. 81 (1984) 3684–3690.
[25] S. Melchionna, G. Ciccotti, B.L. Holian, Mol. Phys. 78 (1993) 533–544.
[26] J.M. Haile, Molecular Dynamics Simulation: Elementary Methods, John Wiley & Sons, Inc., New York, 1992.
[27] H. Tsuzuki, P.S. Branicio, J.P. Rino, Comput. Phys. Commun. 177 (2007) 518–523.
[28] W.K. Luo, H.W. Sheng, F.M. Alamgir, J.M. Bai, J.H. He, E. Ma, Phys. Rev. Lett. 92 (2004) 145502.
[29] N. Jakse, Phys. Rev. Lett. 93 (2004) 207801.
[30] M. Asta, V. Ozolins, J.J. Hoyt, M. van Schilfgaarde, Phys. Rev. B 64 (2001) 20201.
[31] F.C. Frank, J.S. Kasper, Acta Crystallogr. 11 (1958) 184–190.
[32] H.W. Sheng, W.K. Luo, F.M. Alamgir, J.M. Bai, E. Ma, Nature 439 (2006) 419–425.
[33] Y.Q. Cheng, E. Ma, H.W. Sheng, Phys. Rev. Lett. 102 (2009) 245501.
[34] D.R. Nelson, F. Spaepen, Solid State Phys. 42 (1989) 1–90.
[35] S.Q. Wu, C.Z. Wang, S.G. Hao, Z.Z. Zhu, K.M. Ho, Appl. Phys. Lett. 97 (2010) 021901.

[36] D. Ma, A.D. Stoica, X.L. Wang, Nat. Mater. 8 (2008) 30–34.
[37] P. Häussler, Phys. Rep. 222 (1992) 65–143.
[38] H.W. Sheng, H.Z. Liu, Y.Q. Cheng, J. Wen, P.L. Lee, W.K. Luo, S.D. Shastri, E. Ma, Nat. Mater. 6 (2007) 192–197.
[39] S. Wei, I. Gallino, R. Busch, C.A. Angell, Nat. Phys. 7 (2011) 178–182.
[40] C.Z. Zhang, L.N. Hu, Y.Z. Yue, J.C. Mauro, J. Chem. Phys. 133 (2010) 014508.
[41] R. Zallen, The Physics of Amorphous Solids, Wiley, New York, 1983.
[42] W.K. Luo, H.W. Sheng, E. Ma, Appl. Phys. Lett. 89 (2006) 131927.
[43] X.J. Liu, Y. Xu, X. Hui, Z.P. Lu, F. Li, G.L. Chen, J. Lu, C.T. Liu, Phys. Rev. Lett. 105 (2010) 155501.